Lawrence Berkeley National Laboratory
LBL Publications

Title
Model-Based Analysis of the Limiting Mechanisms in the Gas-Phase Oxidation of HCl Employing an Oxygen Depolarized Cathode

Permalink
https://escholarship.org/uc/item/9qd8550m

Journal
Journal of The Electrochemical Society, 167(1)

ISSN
0013-4651

Authors
Bechtel, Simon
Vidaković-Koch, Tanja
Weber, Adam Z
et al.

Publication Date
2020

DOI
10.1149/1945-7111/ab6449

Peer reviewed

OPEN ACCESS

Model-Based Analysis of the Limiting Mechanisms in the Gas-Phase Oxidation of HCl Employing an Oxygen Depolarized Cathode

To cite this article: Simon Bechtel *et al* 2020 *J. Electrochem. Soc.* **167** 013537

View the article online for updates and enhancements.

Model-Based Analysis of the Limiting Mechanisms in the Gas-Phase Oxidation of HCl Employing an Oxygen Depolarized Cathode

Simon Bechtel,[1] Tanja Vidaković-Koch,[2] Adam Z. Weber,[3,*] and Kai Sundmacher[1,4,z]

[1]*Max Planck Institute for Dynamics of Complex Technical Systems, Department Process Systems Engineering, D-39106 Magdeburg, Germany*
[2]*Max Planck Institute for Dynamics of Complex Technical Systems, Electrochemical Energy Conversion Group, D-39106 Magdeburg, Germany*
[3]*Energy Conversion Group, Energy Technologies Area, Lawrence Berkeley National Laboratory, Berkeley, Calforina 94720, United States of America*
[4]*Otto-von-Guericke-University Magdeburg, Department Process Systems Engineering, D-39106 Magdeburg, Germany*

The electrochemical oxidation of HCl to Cl_2 plays an important role in the production of polycarbonates and polyurethanes. Recently, the gas-phase oxidation of HCl proved to be significantly more efficient than the current state-of-the-art process based on the oxidation of hydrochloric acid. In experimental investigations of this gas-phase reactor, a limiting current can be observed that is so far not understood but impedes the overall reactor performance. In the present work, a nonisothermal multiphase agglomerate model is developed to investigate the underlying reasons for this limiting behavior in more detail. It is shown that the thermal management of the cell plays a significant role and that minor changes to its thermal resistance lead to the limiting behavior being caused by either flooding of the cathode or dehydration of the membrane and anode. An optimization of operational and structural parameters of the cell based on these insights leads to an increase in the limiting current by more than 90%. Interestingly, under these conditions a third phenomenon, the rate determining Tafel step in the microkinetic reaction mechanism of the HCl oxidation, limits the overall reactor performance. These insights harbor the potential for enormous energetic savings in this industrially highly relevant process.

Supplementary material for this article is available online

List of Symbols

Temperature	T	K
Wall and feed temperature	T_{in}, T_{wall}	K
Rate constant of Tafel step for the HClOR	k_A	$\frac{mol}{m^3 s}$
standard reaction rate ORR	$k_{ORR}^{\mu,0}$	$\frac{1}{s}$
Henry constant O_2	H_{O_2}	$\frac{Pa\,m^3}{mol}$
Ionomer volume fraction in CL	ϕ_{Nafion}	
Effective diffusion coefficient of oxygen in agglomerates	$D_{O_2}^{\mu,eff}$	$\frac{m^2}{s}$
Oxygen reference concentration at 1 bar partial pressure and 60 K	$c_{O_2,ref}$	$\frac{mol}{m^3}$
Cathode catalyst (Pt) loading	L	$\frac{g}{m^2}$
Activation energy ORR at reversible cell potential	E_c^{rev}	$\frac{J}{mol}$
Reference temperature ORR	T^*	K
Porosity CL	ε_{CL}	
Porosity GDL[1]	ε_{GDL}	
Anode and cathode gas channel pressure	p_{tot}^{GC}	Pa
Effective gas and liquid phase permeability	k_G^{eff}, k_L^{eff}	m^2
Relative gas and liquid phase permeability	$k_{r,G}$, $k_{r,L}$	
Saturated permeability	k_{sat}	m^2
Liquid phase saturation	S_L	
Irreversible liquid phase saturation	$S_{L,irr}$	
Gas phase saturation	S_G	
Exponents for the liquid and gas phase permeability	β_L, β_G	
Capillary pressure	p_c	Pa
Liquid phase pressure	p_L	Pa
Total gas phase pressure	p_G	Pa

(Continued).

Molar mass of water	M_{H_2O}	$\frac{g}{mol}$
Partial pressure of water	p_{H_2O}	Pa
Saturation pressure of water	p_{sat}	Pa
Molar volume of liquid water	V_0	$\frac{m^3}{mol}$
Density of liquid water	ρ_{H_2O}	$\frac{kg}{m^3}$
Anode gas viscosity	$\mu_{g,A} \approx \mu_{HCl}$	Pa s
Cathode gas viscosity	$\mu_{g,C} \approx \mu_{O_2}$	Pa s
Equilibrium constant chloride adsorption/ desorption	K_0	$\frac{m^3}{mol}$
Effective Diffusion coefficient of hydrochloric acid in Nafion	$D_{HCl(aq)}^{\mu,eff}$	$\frac{m^2}{s}$
Agglomerate radius	R_{agg}	nm
Reaction rate on the microscale	r^μ	$\frac{mol}{s\,m^3}$
Activity of species within agglomerates	a_i^μ	$\frac{mol}{m^3}$
Specific internal area of the agglomerates	a^μ	$\frac{m_{active}^2}{m_{agg}^3}$
Overpotential	η	V
Cathode symmetry coefficient	α_c	
Exchange current density ORR	$i_{o,s}$	$\frac{A}{m^2}$
Effectiveness factor in the agglomerates for ORR	E_{ORR}	
Thiele modulus in the agglomerates for ORR	ϕ_{ORR}	
GDL thickness	d_{GDL}	μm
Thickness CL	d_{CL}	μm
Thickness Membrane	d_M	μm
Electrode area	A_{ACL}	m^2
Volumetric flow rate of HCl at standard temperature and pressure (STP)	$\dot{V}_{HCl}$	$\frac{m^3}{s}$
Volumetric flow rate of O_2 at standard temperature and pressure (STP)	$\dot{V}_{O_2}$	$\frac{m^3}{s}$
Pre-factor, Diffusion coefficient of water in Nafion	D_W^0	$\frac{m^2}{s}$
Density of dry membrane	ρ_M	$\frac{kg}{m^3}$

*Electrochemical Society Fellow.
z E-mail: Sundmacher@mpi-magdeburg.mpg.de

(Continued).

Equivalent weight of membrane	EW	$\frac{kg}{mol}$
Concentration of water in membrane	c_W	$\frac{mol}{m^3}$
Membrane water content	λ	
Drag coefficient membrane	ξ	
Water fraction in membrane	f	
Ionic conductivity membrane	κ_M	$\frac{S}{m}$
Molar volume of dry membrane	V_M	$\frac{m^3}{mol}$
Potential loss in membrane	$\Delta\Phi_M$	V
potential loss due to ohmic resistances within the CL, GDL and plate on both sides	ϕ_{RI}	V
Electric current	i	A
plate thickness	d_{plate}	m
PTFE gasket thickness	d_{PTFE}	m
FKM gasket thickness	d_{FKM}	m
Titan endplate thickness	$d_{endplate}$	m
Thermal conductivity endplate	λ_{plate}	$\frac{W}{mK}$
Thermal conductivity plate	λ_{plate}	$\frac{W}{mK}$
Thermal conductivity PTFE gasket	λ_{PTFE}	$\frac{W}{mK}$
Thermal conductivity FKM gasket	λ_{FKM}	$\frac{W}{mK}$
Total thermal resistance	R	$\frac{K}{W}$
Cell potential vs SHE	E_{cell}	V
Open circuit potential	E_{OC}	V
Partial pressure of species i	p_i	Pa
Current density	j	$\frac{A}{m^2}$
Limiting current density	j_{limit}	$\frac{A}{m^2}$
surface coverage of Pt-Cl species	Θ	
Knudson diffusion coefficient of species i	D_{iM}^{eff}	$\frac{m^2}{s}$
Maxwell-Steffan diffusion coeffcients	D_{ij}^{eff}	$\frac{m^2}{s}$
Diffusion coefficients for the inverted solutions of the Maxwell-Steffan equations[a)]	$\overline{D_{ij}}_{eff}$	$\frac{m^2}{s}$
Double layer capacity	C_{DL}	$\frac{F}{m^2}$

a) See supplemental information (stacks.iop.org/JES/167/013537/mmedia).

Chlorine is a crucial educt in the production of numerous chemicals like polyurethanes and polycarbonates.[2,3] Due to the significant growth of these markets, the energy efficient and sustainable recycling of HCl, which is a byproduct of these processes, to Cl_2 is becoming increasingly important.[4] The oxidation of HCl to Cl_2 can be carried out electrochemically (as discussed herein) or heterogeneously catalyzed at high temperatures as in various Deacon-like processes.[4]

The most efficient industrially employed process for the electrolysis of HCl to Cl_2 is the Bayer UHDENORA process, in which aqueous hydrochloric acid is used as a reactor feed.[5,6] As our group recently demonstrated, utilizing a gas-phase reactor as proposed by Kuwertz et al.[7] in combination with novel separation strategies for product purification, leads to exergetic savings of 38% at the overall process level.[5,6,8] A further result of this work was the insight that more than 90% of the exergy demand of the overall gas-phase process is related to the electrochemical reactor and less than 10% to the subsequent separation of unreacted HCl and chlorine.[5] Hence, to further increase the efficiency of this novel process, a better understanding of the gas-phase reactor is required for reactor optimization.

Experiments with a gas-phase reactor carried out by Kuwertz et al.[7] demonstrated a limiting current of 350 to 450 mA cm^{-2} depending on the reactor temperature and cathode feed-gas humidification. An understanding of the underlying causes for this limiting behavior, and possible strategies to mitigate it, are of utmost importance for developing systematic reactor optimization strategies. Interestingly, the half-cell measurements of the

anodic hydrogen chloride oxidation reaction (HClOR) by Martinez et al.[9–11], exhibit a limiting current, which was recently shown to be a purely reaction-limited current.[12] These reaction-limited currents however are clearly higher than the ones observed in the full-cell experiments of Kuwertz et al.[7], in which the anodic HClOR is combined with an oxygen depolarized cathode; they also exhibit a divergent temperature dependence. Hence, the underlying causes of the limiting behavior in the full-cell setup seem to be different.

In a recent review of the HCl gas-phase oxidation,[8] the collective experimental data of Kuwertz and Martinez et al.[7,11] were discussed with respect to indications for the occurrence of flooding in the cathode compartment, as well as for the occurrence of dehydration of the anode catalyst layer (aCL) and the adjacent membrane; both effects that can possibly explain the experimentally observed limiting behavior in the full-cell setup. In the present work, a nonisothermal, 1D thin-film agglomerate model is developed that considers multiphase behavior of water in the cathode compartment in order to further investigate the possible occurrence of flooding and membrane dehydration. Generally, the focus of this work is not a quantitative reproduction of the experiments of Kuwertz et al.[7] but rather a qualitative investigation of the underlying physical mechanisms occurring within the cell. The focus of the mathematical model is to determine the conditions under which the cell is limited, and to develop first strategies to mitigate the limiting influences, paving the way for a more efficient reactor design.

The outline of this paper is as follows. First, the model and the underlying assumptions are explained in detail. This is followed by the interpretation of simulated and experimental polarization curves and the identification of causes for the observed limiting behavior. Finally, the significance of the thermal management of the reactor is investigated, and, based on these insights, optimized operating conditions and structural changes in the reactor are proposed.

Model and Governing Equations

The model herein builds upon our previous anode model[12] by additionally considering multiphase and nonisothermal aspects, and specifically by incorporating a two-phase model of the cathode compartment comprising an oxygen depolarized cathode (ODC) as
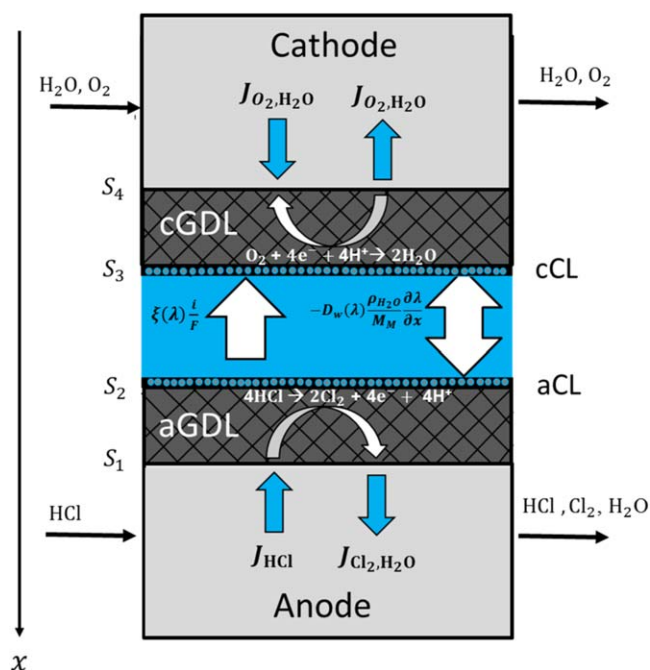

Figure 1. Depiction of the modeling domains aligned with the experiments of Kuwertz et al.[7] The following domains are included in the model: anode gas channel (aGC), anode gas-diffusion layer (aGDL), anode catalyst layer (aCL), Nafion® membrane (M), cathode catalyst layer (cCL), cathode gas-diffusion layer (cGDL) and the cathode gas channel (cGC).

well as a lumped energy balance over the whole cell. The model domains are depicted in Fig. 1. The catalyst layers are described with a thin-film agglomerate model on both sides. Since the model is used for the interpretation of experimental data from Kuwertz et al.,[7] the process conditions and geometrical parameters are adopted from their publications whenever possible.

The following general assumptions are made:

• All gases are treated as ideal gases and the reactor temperature is assumed to be uniform throughout the reactor by employing a lumped energy balance that is not a function of the spatial coordinate. Water in the anode compartment of the cell is assumed to be in its gaseous state only, while in the cathode compartment a two-phase model is employed.

• Condensation and evaporation of water is assumed to be fast due to large enough interfacial area so that local equilibrium can be assumed at all times.

• The membrane is modeled as impermeable for all species besides water and protons.

• The gaseous HCl is absorbed and dissociates within the water containing agglomerates of the catalyst layer. Hence, the expressions for the reaction kinetics are based on the activity of the aqueous Cl^- species.

Species considered in the anode compartment of the cell are HCl, Cl_2 and gaseous H_2O, while in the cathode compartment O_2 and H_2O are allowed. H_2O is restricted to its gaseous state in the cGC, whereas both liquid and gaseous states are accounted for in the cGDL and cCL. Like in the experiments of Kuwertz et al,[7] the cathode feed humidity is essentially at 100% RH, small reductions being made in order to facilitate convergence, while the anode feed consists of pure HCl. The governing equations and boundary conditions are summarized in Tables I and II, respectively, and further explained below.

Energy balance.—Contrary to the mass balance of the reactants and products, the energy balance is not discretized in the direction of the x coordinate (see Fig. 1) but treated as a single lumped balance over the whole reactor (Eq. 8).[13,14] The values for all parameters are given in Table III and are based on the properties of the reactor employed in the experiments of Kuwertz et al.[7] The thermal resistance R of the reactor, considering the heat transfer through the plate, the PTFE gasket the FKM gasket and the titanium endplate, is calculated as

$$R = 0.5\left(\frac{d_{plate}}{A\lambda_{plate}} + \frac{d_{PTFE}}{A\lambda_{PTFE}} + \frac{d_{FKM}}{A\lambda_{FKM}} + \frac{d_{endplate}}{A\lambda_{endplate}}\right) \quad [9]$$

where the surface of the plate facing the GDL is assumed to be at thermal equilibrium with the inside of the reactor having a temperature of $T = T_R$. The factor of 0.5 is a consequence of the simultaneous heat transfer through both the anode and cathode side. Contact resistances between the above mentioned layers are neglected in the model.

More information on the exact structure of the reactor can be found in Ref. 7. The values for the according conductivities and layer thicknesses are listed in Table III. Please note that the thickness of the titanium endplate is not given in Ref. 7 but is estimated to be 0.5 cm from unpublished pictures of the reactor setup. Furthermore, it is important to note that the thermal resistance R in Eq. 9 does not include heat transfer from the titanium endplate into the cooling medium, which is flowing through that plate and has the same temperature as the reactor feed gases in the setup of of Kuwertz et al.[7] This is based on the fact that the exact thickness of the titanium plate, the area in contact with the cooling media and its flowrate in the experiments of Kuwertz et al.[7] are unknown. Also, the possibility of heat transfer to the ambient air surrounding the reactor via the surface area not in contact with the cooling medium is not included in the model for the same reasons.

Gas-phase mass transport.—As in Ref. 12, the anode and cathode gas channel are treated as perfectly mixed compartments (Eq. 1). The diffusive mass transfer of all gaseous species within the GDL is described by the multicomponent Stefan-Maxwell equations,[28] while

the convective mass transfer is modeled based on Darcy's law and the conservation of mass (Eqs. 2, 3, respectively).[29] Additionally, the effect of pressure-diffusion is considered in the cGDL, since water condensation can lead to higher pressure losses compared to the anode side, which might be a considerable driving force for mass transfer under certain conditions (Eq. 3).[29]

As in Ref. 29,30 the effective gas phase permeability k_G^{eff} is calculated as a product of the relative gas-phase permeability $k_{r,G}$ and saturated permeability k_{sat}. Since all water in the anode compartment is assumed to be in its gaseous state, the relative permeability is fixed to be one in the aGDL.

$$k_G^{eff} = k_{sat}k_{r,G} = k_{sat}(1 - S_{L,GDL})^{\beta_G} \quad [10]$$

where S_L is the liquid-phase saturation. The values for the exponent β_G and the saturated permeability k_{sat} were extracted from[29] and are given in Table III.

The effective diffusion coefficient can be modeled according to the Bruggeman correlation:

$$\overline{D_{ij}}_{eff} = \overline{D_{ij}}\varepsilon^{1.5} \quad [11]$$

Where $\overline{D_{ij}}$ is a function of the Stefan-Maxwell diffusion coefficients.[29,31] More detailed information on their calculation is given in the supplemental information (stacks.iop.org/JES/167/013537/mmedia). As boundary conditions, the continuity of partial pressures at the GC|GDL interface and the GDL|CL interface are chosen, as listed in Table II.

Two-phase modeling of water in the cGDL.—Due to the assumption of local equilibrium between gaseous and liquid water, the mass transfer of water in both phases (Eq. 4) can be described with a single equation so that rate terms describing evaporation and condensation can be omitted. The benefits of choosing this approach are a better convergence and lower simulation costs, since n ODEs, with n being the number of discretization cells in the cGDL, can be omitted. This assumption is justified by studies showing that water in both the gas and liquid phase are essentially in equilibrium due to the extended vapor/liquid interfacial areas and rapid phase-change kinetics in the CL and GDL leading to a fast evaporation and condensation rate.[19,32,33]

In this case, the liquid-water pressure can be calculated from the partial pressure of water by setting the chemical potentials in both phases equal, leading to

$$p_L - p_G = p_c = \frac{RT \, ln\left(\frac{p_{H_2O}}{p_{sat}}\right)}{V_0 + \frac{M_{H_2O}}{RT\rho_{H_2O}}} \quad [12]$$

where the curvature of water droplets is considered by means of the Kelvin equation.[30] However, Since $V_0 = \frac{M_{H_2O}}{\rho_{H_2O}}$ and $1 \gg \frac{1}{RT}$ Eq. 12 can be simplified

$$p_L = p_G + \frac{RT\rho_{H_2O} \, log\left(\frac{p_{H_2O}}{p_{sat}}\right)}{M_{H_2O}} \quad [13]$$

The transport of both liquid and gaseous water is then combined in Eq. 4, with the transport of gaseous water being modeled as discussed above for all other gas species, and the convective transport in the liquid phase being described by Darcy's law. Similar to the gas-phase permeability, the liquid-phase permeability is calculated as in Ref. 29

$$k_L^{eff} = k_{sat}k_{r,L} = k_{sat}(S_{L,GDL} - S_{L,GDL,\,irr})^{\beta_L} \quad [14]$$

with $S_{L,GDL,irr}$ being the irreversible liquid-phase saturation, which takes isolated domains filled with water into account that do not participate in the convective mass transport.[29]

Table I. Governing equations in the gas channel, GDL and membrane.

Variable	Governing equation	Eq.	Region
Partial pressure	$$V\frac{dP_\alpha^{GC}}{dt} = (\dot{V}_{in}P_{\alpha,in}^{GC} - \dot{V}_{out}P_\alpha^{GC}) + RTJ_\alpha|_{S1,t}$$	1	GC
Partial pressure of gaseous species in Anode compartment	$$\frac{\partial P_i^{AGDL}}{\partial t} = -\nabla\left[\frac{P_{tot}}{RT}\sum_{j\neq i}\overline{D_{ij}}_{eff}\nabla\frac{P_j^{AGDL}}{P_{tot,A}}\right] + \frac{k_{eff,g}}{\mu_{g,A}}\nabla(P_i^{AGDL}\nabla p_{tot,A})$$	2	aGDL
Partial pressure of O_2 in Cathode compartment	$$\frac{\partial P_{O_2}^{CGDL}}{\partial t} = \left[\frac{P_{tot,C}}{RT}D_{H_2O-O_2\,eff}\nabla\frac{P_{O_2}^{CGDL}}{p_{tot,C}}\right.$$ $$+ \frac{D_{H_2O-O_2\,eff}}{RT}\left(\frac{P_{O_2}^{CGDL}}{p_{tot,C}} - \frac{P_{O_2}^{CGDL}M_{O_2}}{P_{G,H_2O}^{CGDL}M_{H_2O} + P_{O_2}^{CGDL}M_{O_2}}\right)\nabla p_{tot,C}\left.\right]$$ $$+ \frac{k_{eff,g}}{\mu_{g,C}}\nabla(P_{O_2}^{CGDL}\nabla p_{tot,C})$$	3	cGDL
Partial pressure of H_2O in Cathode compartment	$$\frac{\partial P_{G,H_2O}^{CGDL}}{\partial t} = \left[\frac{P_{tot,C}}{RT}D_{H_2O-O_2\,eff}\nabla\frac{P_{G,H_2O}^{GCDL}}{p_{tot,C}}\right.$$ $$+ \frac{D_{H_2O-O_2\,eff}}{RT}\left(\frac{P_{G,H_2O}^{GCDL}}{p_{tot,C}} - \frac{P_{G,H_2O}^{CGDL}M_{H_2O}}{P_{G,H_2O}^{CGDL}M_{H_2O} + P_{O_2}^{CGDL}M_{O_2}}\right)\nabla p_{tot,C}\left.\right]$$ $$+ \frac{k_{eff,g}}{\mu_{g,C}}\nabla(P_{G,H_2O}^{GDL}\nabla p_{tot}) + \nabla\left(\frac{RTc_{H_2O,L}}{\mu_{H_2O,L}}k_{eff,L}\nabla p_{L,H_2O}\right)$$	4	cGDL
Water content in membrane	$$\frac{\partial\lambda_M}{\partial t} = +D_W(\lambda_M)\Delta\lambda_M + \frac{M_W}{\rho_W}\nabla\xi(\lambda_M)\frac{i}{F}$$	5	Membrane
Chloride ion concentration within agglomerate	$$\frac{\partial c_{Cl^-}}{\partial t} = -\frac{1}{r^2}\frac{\partial}{\partial r}\left(r^2 D_{HCl(aq)}^{\mu,eff}\frac{\partial c_{Cl^-}}{\partial r}\right) + a^\mu\upsilon_{Cl}\,r_i^\mu(a_{Cl^-}^\mu, \eta,)$$	6	Agglomerates in aCL
Anode and cathode overpotential	$$\frac{d\eta}{dt} = \frac{i + d_{CL}J_i^\mu F}{C_{DL}}$$	7	aCL and cCL
Temperature	$$T_r = \frac{-\Delta_R h*(G_{in}^A*x_{HCl,in}^A - G_{out}^A*x_{HCl,out}^A) - P_{el} + \frac{T_{wall}}{R} + T_{in}*(G_{in}^A*C_{p,in}^A + G_{in}^C*C_{p,in}^C)}{\frac{1}{R} + (G_{in}^A*C_{p,in}^A + G_{in}^C*C_{p,in}^C)}$$	8	Whole cell

Table II. Boundary conditions.

Variable	Boundary condition	Boundary
Partial pressure gas phase	$p_i^{GDL}\|_{x=S1,S3,t} = p_i^{GC}$	aGC|aGDL and cGC|cGDL
Partial pressure gas phase	$J_i\|_{x=S2,t} = d_{ACL}J_{i,A}^{\mu}$ $J_i\|_{x=S3,t} = d_{CCL}J_{i,C}^{\mu}$	aGDL|aCL and cGDL|cCL
Total pressure gas phase	$p_{tot}^{GDL}\|_{x=S1,S4,t} = p_{tot}^{GC} = 1\ bar$	aGC|aGDL and cGC|cGDL
Total pressure gas phase	$\left(\dfrac{p_{tot}k_{eff,g}}{\mu_g}\nabla p_{tot}\right)\Bigg\|_{x=S2,S3,t} = s_{tot}$	aGDL|aCL and cGDL|cCL
Liquid pressure in cathode compartment	$p_L^{GDL}\|_{x=S4,t} = p_{tot}^{CGC}$ for $p_L^{GDL} \geqslant p_{tot}^{CGC}$ And $J_L\|_{x=S4,t} = 0$ for $p_L^{GDL} \geqslant p_{tot}^{CGC}$	cGC|cGDL
Liquid pressure in cathode compartment	$p_L^{GDL}\|_{x=S4,t} = p_L^{CL}$	cGDL|cCL
Water content membrane	$\lambda_M\|_{x=S3,t} = \lambda_{CCL}$ $= (1-S)\left[0.043 + 17.81\dfrac{P_{H_2O}^{CCL}}{P_{sat}} - 39.85\left(\dfrac{P_{H_2O}^{CCL}}{P_{sat}}\right)^2 + 36\left(\dfrac{P_{H_2O}^{CCL}}{P_{sat}}\right)^3\right]$ $+ 17S$	cCL|M
Water content membrane	$\lambda_M\|_{x=S2,t} = \lambda_{ACL} = 0.043 + 17.81\dfrac{P_{H_2O}^{ACL}}{P_{sat}} - 39.85\left(\dfrac{P_{H_2O}^{ACL}}{P_{sat}}\right)^2 + 36\left(\dfrac{P_{H_2O}^{ACL}}{P_{sat}}\right)^3$	M|aCL
Chloride ion activity at the surface of anode agglomerates	$a_{Cl^-}{}^{\mu}(r = R) = f(T, P_{HCl}^{ACL})$	aCL|Agglomerate
Chloride ion flux in the center of anode agglomerates	$J_{Cl^-}^{\mu}(r = 0) = 0$	Agglomerate center

Table III. Model parameters implemented in the reactor simulation.

Parameter	Symbol	Value	Unit
Wall and feed temperature	T_{in}, T_{wall}	—	K
Rate constant of Tafel step for the HClOR	k_A	$k_A = \frac{ECSA_{rel}(\lambda)}{ECSA_{rel}(\lambda = 4)}32.188e^{0.01788T}$	$\frac{mol}{m^3 s}$
standard reaction rate ORR	$k_{ORR}^{\mu,0}$	22.227	$\frac{1}{s}$
Henry constant O_2[15]	H_{O_2}	$H_{O_2} = 0.1e^{\left(14.1 - \frac{666}{T}\right)}$	$\frac{Pa\,m^3}{mol}$
Ionomer volume fraction in CL	ϕ_{Nafion}	0.374	
Effective diffusion coefficient of oxygen in agglomerates[16]	$D_{O_2}^{\mu,eff}$	$D_{O_2 - H_2O}^{\mu,eff} = \phi_{Nafion}^{1.5}24.82e^{\frac{-1949}{T}}$	$\frac{m^2}{s}$
Oxygen reference concentration at 1 bar partial pressure and 60 K	$c_{O_2,\,ref}$	5.5545	$\frac{mol}{m^3}$
Cathode catalyst (Pt) loading	L	5	$\frac{g}{m^2}$
Activation energy ORR at reversible cell potential[17]	E_c^{rev}	67000	$\frac{J}{mol}$
Reference temperature ORR[17]	T^*	353.15	K
Porosity CL	ε_{CL}	0.6	
Porosity GDL[18]	ε_{GDL}	0.75	
Anode and cathode Gas channel pressure	p_{tot}^{GC}	100000	Pa
saturated permeability[19]	k_{sat}	$1.54 \cdot 10^{-15}$	m^2
Exponents for the liquid and gas phase permeability[19]	β_L, β_G	3.5	
Anode gas viscosity[20]	$\mu_{g,A} \approx \mu_{HCl}$	$\mu_{HCl} = (-9.188 + 0.555T - 0.000113T^2)10^{-7}$	Pa s
Cathode gas viscosity[20]	$\mu_{g,C} \approx \mu_{O_2}$	$\mu_{O_2} = (44.224 + 0.562T - 0.00011T^2)10^{-7}$	Pa s
Equilibrium constant chloride adsorption/desorption	K_0	$K(T) = 584684.86e^{-\frac{75497.5}{RT}}$	$\frac{m^3}{mol}$
Effective Diffusion coefficient of hydrochloric acid in Nafion[21]	$D_{HCl(aq)}^{\mu,eff}$	$\phi_{Nafion}^{1.5}1.2 \cdot 10^{-11}$	$\frac{m^2}{s}$
Agglomerate radius[15]	R_{agg}	200	nm
GDL thickness[18]	L_{GDL}	400	μm
Thickness CL[7]	L_{ACL}	10	μm
Thickness Membrane[11]	L_M	178	μm
Electrode area[7]	A_{ACL}	$3 \cdot 10^{-3}$	m^2
Volumetric flow rate of HCl at standard temperature and pressure (STP)[7]	$\dot{V}_{HCl}$	$10 \cdot 10^{-6}$	$\frac{m^3}{s}$
Volumetric flow rate of O_2 at standard temperature and pressure (STP)[7]	$\dot{V}_{O_2}$	$10 \cdot 10^{-6}$	
Pre-factor, Diffusion coefficient of water in Nafion[22]	D_W^0	$2.1 \cdot 10^{-7}$	$\frac{m^2}{s}$
Density of dry membrane[47]	ρ_M	2000	$\frac{kg}{m^3}$
Equivalent weight of membrane[23]	EW	1.1	$\frac{kg}{mol}$
Drag coefficient membrane[24]	ξ	3.5 at full membrane hydration	
plate thickness[7]	d_{plate}	0.0057	m
PTFE gasket thickness[7]	d_{PTFE}	0.00012	m
FKM gasket thickness[7]	d_{FKM}	0.0005	m
Titan endplate thickness	$d_{endplate}$	0.005	m
Thermal conductivity endplate	λ_{plate}	15.6	$\frac{W}{mK}$
Thermal conductivity plate[25]	λ_{plate}	20	$\frac{W}{mK}$
Thermal conductivity PTFE gasket[26]	λ_{PTFE}	0.245	$\frac{W}{mK}$
Thermal conductivity FKM gasket[27]	λ_{FKM}	0.75	$\frac{W}{mK}$
Total thermal resistance	R	0.294	$\frac{K}{W}$

The liquid-phase saturation is calculated based on experimental data from Gostick et al.[34] relating $S_{L,GDL}$ to the capillary pressure for a GDL consisting of Toray 090 Paper. The following fit-function was developed to obtain an equation for the saturation as a function of the capillary pressure,

$$S_{L,GDL} = 0.48 \tanh\left(\frac{p_C - 2500}{8000} + 1\right) + 0.0358 \qquad [15]$$

Both the fit-function as well as the corresponding experimental data are displayed in Fig. 2. Please note that Kuwertz et al.[7] used a different GDL material than[34] so that slight deviations between the actual and simulated properties cannot be avoided. However, since the goal of the present work is a qualitative evaluation of phenomena causing the observed limiting behavior this uncertainty is acceptable, especially since carbon-based GDL properties are not expected to vary that significantly.
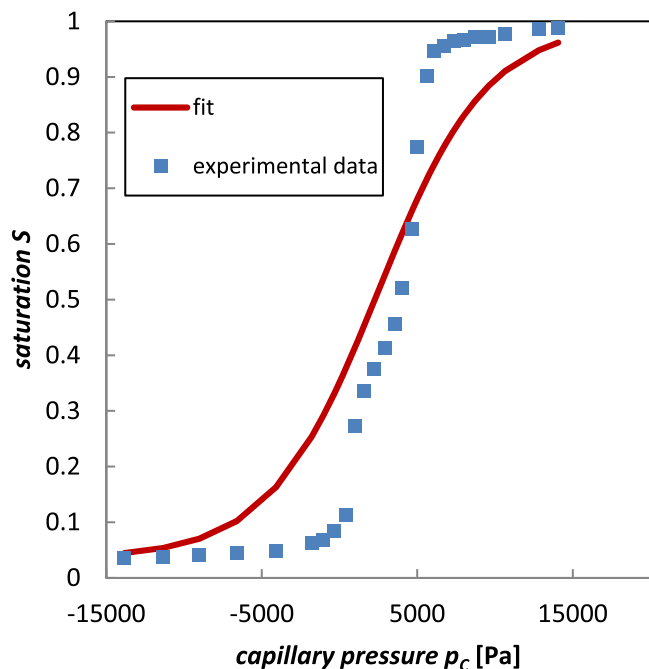
Figure 2. Experimentally determined[32] and fitted saturation within the GDL as a function of the capillary pressure.

The same procedure was chosen for obtaining a fit for the saturation $S_{L,CL}$ in the cCL employing experimental data from Kusoglu et al.,[35]

$$S_{L,CL} = 0.405 \tanh\left(\frac{p_C - 3000}{8000} + 1\right) + 0.18 \qquad [16]$$

Both the data and the fit-function are displayed in Fig. 3.

As a boundary condition, the partial pressure of water at the cGC|cGDL interface is set equal to its value in the cathode gas channel, identical to the treatment of other gas species. For the liquid-phase transport, a no-flux condition is enforced as long as the liquid pressure at the boundary between cGDL and cGC does not exceed the total gas pressure in the cGC. This is based on the assumption that there are no liquid-water reservoirs in the cGC, so that no liquid flux
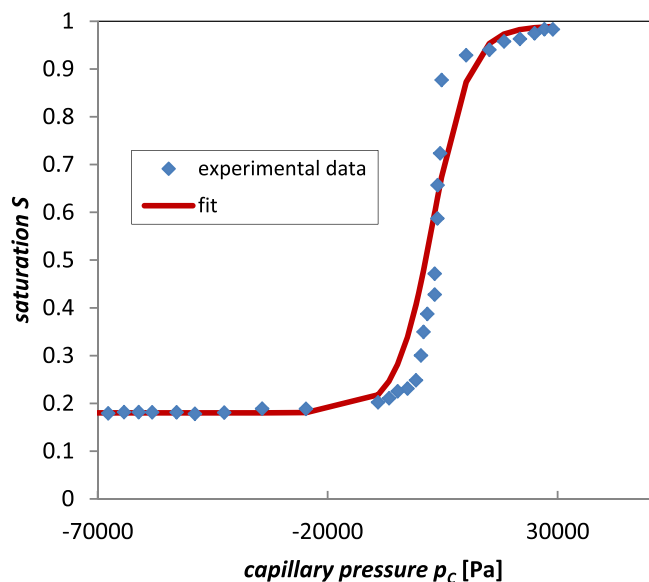

Figure 3. Experimentally determined[33] and fitted saturation within the CL as a function of the capillary pressure.

from the GC into the cGDL is allowed.[29] At liquid pressures greater than the total gas pressure, they are set equal to the total gas pressure. Please note that this is not a classical boundary condition, since the equilibrium assumption entails the need of only one boundary condition due to the equilibrium expression replacing the other one, as discussed above. However, since both the partial pressure of water and the liquid pressure are directly coupled, solving for the partial pressure by the above described scheme leads to identical results as solving for the liquid pressure with the no-flux condition enforced as a classical boundary condition and a simple continuity assumption for the partial pressure at the cGC|cGDL interface.

Membrane.—The membrane model is identical to the one employed in our previous work 12, with the only difference being the determination of the ionic conductivity according to Eq. 17. The water transport is described by three different mechanism that are electroosmosis, diffusion, and a hydraulic flux as proposed by Eikerling et al.,[36] where the latter two mechanisms are combined in an effective diffusion coefficient D_W as depicted in Eq. 5. It should be noted that the equilibrium water content of the membrane in contact with liquid water was defined as 17. This is clearly lower than the classical value of 22 that is employed in most PEM fuel cell studies. The reason for this is the presence of hydrochloric acid in the aCL and it's permeation into the membrane. Balko et al.[37] have shown that a membrane in contact with hydrochloric acid exhibits equilibrium water contents that strongly decrease with higher acid concentrations and that can go down to values of 5,[37] as the water activity is suppressed in HCl solutions.[38–40] Since in the reactor model and the experiments of Kuwertz et al.,[7] hydrochloric acid is only present on one side of the membrane and it is not clear to which extent it permeates through the membrane or impacts water content if it does, an average value of 17 between the water content determined by Balko et al.[37] at typical acid concentrations present in the HCl gas-phase electrolysis and the value of 22 for membranes in contact with pure water is chosen. This is identical to the value already employed in our previous work.[12]

The ionic conductivity is calculated as follows

$$\kappa_M = \kappa_{M,0}(f - 0.042)^{0.88} = 50e^{\frac{15000}{R}\left(\frac{1}{303.15} - \frac{1}{T}\right)}(f - 0.042)^{0.88}$$
$$[17]$$

With f being the volume fraction of water in the membrane,

$$f = \frac{V_0 \lambda_M}{V_0 \lambda_M + V_M} \qquad [18]$$

assuming additive molar volumes, where V_0 is the molar volume of water and $V_M = \frac{EW}{\rho_M}$ is the molar volume of the polymer, with *EW* being the equivalent weight of the membrane (please see Table III). Here, the experimentally determined percolation threshold of 0.042 and exponent of 0.88 for a Nafion® 117 membrane from the work of Ochi et al.[41] is employed. The temperature dependence of the ionic conductivity is included in κ_0 for which the expression in the second half of Eq. 17, proposed by Weber et al.,[42] is used. As boundary conditions, continuity of the water content in direction of the both the aCL and cCL is assumed (Table II).

The potential loss within the ionomer can then be calculated as[12]

$$\Delta\Phi_M = i\left(\int_0^{d_M} \frac{dx}{\kappa_M(\lambda_M)}\right) \qquad [19]$$

Here the contribution of the aCL and cCL to the proton conduction is neglected. Since the membrane employed in the experiments of Kuwertz et al.[7] is 18 times thicker than the catalyst layers, this is a good approximation under most conditions. When the aCL and adjacent membrane is dehydrating, it is possible that neglecting the aCl contribution to the proton conduction leads to inaccuracies. In order to consider this contribution, the catalyst layer would have to be discretized. Then the electrical and ionic resistance in the CL can

both be accounted for, weighted by an average reaction location within the CL that can be derived from a transmission line approach as discussed for example in Ref. 43,44. Since the CL is treated as a thin film with a spatially constant overpotential in the present model, this approach is not feasible at the current state for numerical reasons but should be part of future investigations.

Catalyst layer and reaction kinetics.—On the macroscale, the anode and cathode catalyst layer are modeled stationary as a thin film, while on the microscale, an agglomerate model is employed. Hence, the catalyst layer is described by the balances of fluxes entering and leaving from both sides as listed in Table II.[12] For more information on the concept of the agglomerate model, the reader may refer to.[45] From these algebraic equations, the partial pressure of all gaseous species and the total pressure and the water content in the aCL and cCL can be calculated. The source term s_{tot} in the boundary condition for the total pressure (Table II) includes the fluxes J_i^μ into and out of the agglomerates, and additionally the water flux at the CL|M interface as well as the diffusive and convective flux of all gaseous species and, on the cathode side, the liquid water flux on the cGDL|cCL interface. Due to the presence of liquid water, this equation has to be adjusted on the cathode side so that it only accounts for the portion of water in the cCL that is in its gaseous state, since the liquid portion does not contribute to the gas-phase pressure. Hence, this liquid portion is discriminated by multiplying the water flux at the cGDL|cCL and the cCL|M interface with a factor of $(1 - S_{L,CCL})$. The underlying assumption is that at full saturation, all water will be in the liquid phase, at zero saturation, all water will be in the gas phase, and at saturations in-between these two limits, the portion is split between both phases by employing the above mentioned factor. The necessity of such an approach arises from the use of only one equation for describing the water flux due to the assumed phase equilibrium.

The fluxes J_i^μ into and out of the agglomerates can be calculated based on the reaction rate averaged over the whole agglomerate,[45]

$$J_i^\mu = -\frac{1}{R_{agg}^2} a \int_{r=0}^{r=R_{agg}} r^2 a^\mu r^\mu (a_i^\mu, \eta) dr \qquad [20]$$

where R_{agg} is defined as the radius of the agglomerates, $a = \frac{3}{R_{agg}}(1 - \varepsilon_{CL})$, r^μ is the reaction rate on the microscale, a^μ the specific internal area of the agglomerates in $\frac{m_{act}^2}{m_{agg}^3}$, and a_i^μ the activity of the species i within the agglomerate.[45]

To solve Eq. 20, the activity a_i^μ of species i within the agglomerate as a function of the spatial coordinate r must be determined by solving the mass balance on the microscale depicted in Eq. 6. For the HClOR, the rate expression derived in Ref. 12 is employed,

$$i^\mu = 2Fk_A \left(\frac{K_0 a_{Cl^-}}{1 + K_0 a_{Cl^-} e^{\frac{F\eta}{RT}}} \right)^2 e^{\frac{2F\eta}{RT}} (1 - e^{\frac{-2F\eta}{RT}}) \qquad [21]$$

The temperature dependence of the rate constant k_A and the equilibrium constant for the adsorption and desorption of chloride ions is expressed in an Arrhenius form with the activation energy and pre-factor fit to the experimentally determined reaction-limited current densities from the HCLOR experiments of Martinez et al.[11] (see supplemental information for a graphical representation). A similar procedure was followed for describing the temperature dependence of K_0 utilizing the values determined in our previous publication[12] for generating a fit. Since the experiments of Kuwertz et al.[7] were carried out using a different loading, which according to half-cell measurements of the HClOR by Martinez et al.[11] leads to a reduction in the reaction limited current of ca. 11%, the rate constant employed in the present work was corrected with a factor of 0.89 compared to the ones obtained in our earlier work focusing on the anodic HCl oxidation.[12] This correction and the justification of the above mentioned Arrhenius fit using Martinez' experimental limiting

current data[11] is based on the fact that the limiting behavior in these experiments was shown to be caused by the rate determining Tafel step in the HClOR mechanism limiting the overall reaction rate. As a consequence, the rate constant of the HClOR is directly proportional to the reaction limited current as described in Eq. 30 of our previous work[12] allowing for the above mentioned adjustments of the rate constant derived from the experimental limiting current density data.

Lastly, Zhu et al.[1] have shown that the electrochemically available surface area (ECSA) in PEM fuel cells is heavily dependent on the water content at low humidity ($\lambda < 3$). While this is irrelevant for the half-cell model of the HClOR presented in our previous work due to sufficient hydration, the change of ECSA with the water content is considered on the anode side due to possible dehydration. This is done by creating a fit for the ECSA as a function of the water content based on the experimental data by Zhu et al.[1], and using the water content at the limiting current in the half-cell model of our previous work as a reference to then determine the rate constant, which is proportional to the ECSA, at any given water content in the present model (please see supplemental information for more details).

Employing the kinetic expression in Eqs. 21, 5 and 20 are solved numerically for the HClOR, since an analytical solution is untenable. As the first boundary condition, a vapor-liquid-equilibrium between HCl in the gas phase and in the water containing agglomerates is assumed at the surface ($r = R$) as discussed in more detail in.[12] The employed fit function describing the mole fractions and activity coefficients of dissolved chloride anions on the agglomerate surface in dependence on the HCl partial pressure and the temperature is given in the supplemental information together with the experimental data from previous literature on which the fit is based. The second boundary condition consists of a no-flux criteria in the center of the spherical agglomerate ($r = 0$) for reasons of symmetry.

For the ORR however, the following analytical solution for Eq. 20 can be employed assuming first-order reaction kinetics as described in more detail in Refs. 19,45,17

$$J_{O_2}^\mu = \frac{p_{O_2, CCL}}{H_{O_2}} \left(\frac{1}{k_{ORR}^\mu E_{ORR}(1 - \varepsilon_{CCL})} + \frac{\delta}{D_{O_2}^{\mu,eff}} \frac{R}{3(1 - \varepsilon_{CCL})} \right)^{-1}$$

$$[22]$$

$$E_{ORR} = \frac{1}{\phi_{ORR}} \left(\frac{1}{\tanh(3\phi_{ORR})} - \frac{\phi_{ORR}}{3} \right) \qquad [23]$$

$$\phi_{ORR} = \frac{3}{R_{agg}} \sqrt{\frac{k_{ORR}^\mu}{D_{O_2-H_2O}^{\mu,eff}}} \qquad [24]$$

Where E_{ORR} is the effectiveness factor, ϕ_{ORR} the Thiele modulus and

$$k_{ORR}^\mu = (1 - S_{L,CCL}) a^\mu \frac{i_{o,s}}{4Fc_{O_2, ref}} \exp\left(\frac{-\alpha_c F}{RT} \eta_C \right) \qquad [25]$$

and

$$i_{o,s} = i_{o,s}^* \exp\left(-\frac{E_c^{rev}}{RT} \left(1 - \frac{T}{T^*} \right) \right) \qquad [26]$$

according to a Tafel equation proposed by Gasteiger et al.[17] with E_c^{rev} being the activation energy of the ORR at the reversible cell potential. Inserting Eq. 26 into Eq. 25 gives

$$k_{ORR}^\mu = (1 - S_{L,CCL}) \frac{a^\mu i_{o,s}^*}{4Fc_{O_2, ref}} \exp\left(\frac{-\alpha_c F}{RT} \eta_C - \frac{E_c^{rev}}{RT} \left(1 - \frac{T}{T^*} \right) \right)$$

$$= (1 - S_{L,CCL}) \frac{k_{ORR}^{\mu,0}}{4F} \exp\left(\frac{-\alpha_c F}{RT} \eta_C - \frac{E_c^{rev}}{RT} \left(1 - \frac{T}{T^*} \right) \right) \qquad [27]$$

where the term $\frac{a^\mu i_{o,s}^*}{c_{O_2, ref}}$, with $c_{O_2, ref}$ being the reference concentration of O_2 in the agglomerate, is summarized in the catalyst specific

standard rate constant $k_{ORR}^{\mu,0}$ in units of $\frac{1}{s}$, whose value is given in Table III.

Finally, the charge balance for the double layer of anode and cathode is formulated with the electrode double layers acting as a capacitor and the charge transfer acting as an ohmic resistance in parallel according to Eq. 7.[12] Here, C_{DL} is the capacity of the double layer and d_{CL} the catalyst layer thickness. The overall cell potential is calculated as

$$E_{cell} = -(E_{OC} + \eta_A - \eta_C + \phi_M + \phi_{RI}) \qquad [28]$$

where ϕ_{RI} is the potential loss due to ohmic resistances within the CL, GDL and plate on both the anode and cathode sides,

$$\phi_{RI} = 2i\left(\frac{d_{CL}}{\sigma_{CL}} + \frac{d_{GDL}}{\sigma_{GDL}} + \frac{d_{plate}}{\sigma_{plate}}\right) \qquad [29]$$

The electronic conductivities σ_i and thicknesses of all layers d_i are given in Table III. The contact resistance between the different layers is neglected due to its assumed small impact. The temperature-dependent values for the open-circuit potential U_{OCP} are adopted from the experimental work of Kuwertz et al.[18] This indirectly accounts for effects like the poisoning of the cathode catalyst as a consequence of crossed over HCl/Cl$_2$, which are leading to the OCP of the ORR within the setup of Kuwertz et al.,[7,18] being lower than what is commonly seen in classical proton-exchange-membrane fuel cells [46].

Numerical methods and parameters.—The differential equations discussed in the previous sections are discretized based on the finite volume method employing 40 discretization cells in simulations where membrane dehydration can occur and 20 cells in simulations with well hydrated membranes, except for the agglomerates which always contain 10 discretization cells only. The obtained ODEs together with the algebraic equations listed in Tables I and II are solved in MATLAB R2015b using the ode15s solver. The standard rate constant $k_{ORR}^{\mu,0}$, or to be more precise, the active catalyst area per cubic meter of agglomerate a$^\mu$, which is contained in the standard rate constant, is the only fitting parameter in the model. All other parameters are taken from literature to ensure that the model is physically realistic and predictive and that agreement with experimental data is not just a consequence of various fit parameters.

Results and Discussion

Polarization curves and physical mechanisms explaining the observed limiting behavior.—In the following, the simulated polarization curves for temperatures of 313, 323 and 333 K, referring to the temperatures of the coolant and the reactor feed as in the experiments of Kuwertz et al.,[7] are discussed.

A qualitative comparison of the simulated polarization curves in Fig. 4 with the experimental data of Kuwertz et al.[7] shows that their limiting currents at intermediate current densities between 4000–5000 A m^{-2} are reproduced by the model, even though the range of the limiting currents of 2000–5700 A m^{-2} in the simulation results is clearly wider.

The quantitative differences can likely be explained by four major factors: The uncertainties in the structural and operational parameters of the experimental reactor concerning the heat removal as explained above; the use of literature values for all model parameters, with the exception for the active catalyst area and hence the rate constant of the ORR; the assumption of a one-dimensional reactor, which neglects reactant depletion and water accumulation along the channel; and possibly the use of the lumped energy balance.

Furthermore, the sequence in the values of the limiting current densities for the three investigated temperatures is different in the experiments of Kuwertz et al.,[7] with the 333 K experiment
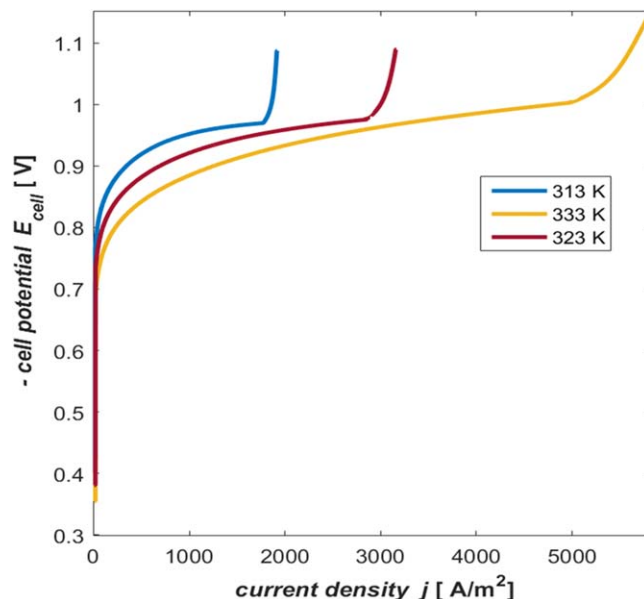

Figure 4. Simulated polarization curves at 313, 323 and 333 K based on the conditions in the experiments of Kuwertz et al.[7] discussed in the model section. The slight discontinuities at the onset of the limiting currents are due to the solution switching between a partially saturated and non-saturated state as a consequence of the flooding process leading to numerical artefacts.

displaying the lowest and the 313 K case displaying the highest limiting current density. This is likely due to the fact that heat transfer to the surrounding air is not considered in the model for reasons discussed above. Especially for the simulations at higher feed and reactor temperatures, this component of the heat transfer becomes more important as the temperature gradient to the environment increases while the temperature of the cooling medium is adjusted according to the feed temperature. Hence, neglecting the heat transfer towards the surrounding air leads to a stronger overestimation of the overall thermal resistance at higher reactor temperatures and therefore to an overestimation of the reactor temperature with rising current densities compared to the simulations at lower starting temperatures. The greater accumulation of heat in turn postpones flooding to higher current densities as discussed in more detail below, explaining why the limiting current density increases with temperature in the simulation but not in the experimental investigations of Kuwertz et al.[7]

Irrespective of these quantitative differences, the focus is on the underlying physics that lead to the phenomena observed in the simulated and experimental polarization curves, as discussed in more detail below, and not obtaining a best fit.

From the polarization curves (both experimental and simulated), one can see a small slope in the ohmic regime at 313 and 323 K, with a markedly steeper slope at 333 K. In addition, the more limiting current onset is more abrupt and steep in the case of the two lower temperatures compared to the 333 K case. The origin of these phenomena becomes clear when looking at the water content in the aCL and cCL as a function of the current density for the lowest and highest investigated temperature as depicted in Fig. 5.

The water content in the aCL and cCL at both temperatures is increasing with the current density, reaching a value of 14 on the cathode side, at which water condensation is initiated, and then going up to a value of 17 corresponding to full saturation and flooding of the cCL. Hence, the first major conclusion to be drawn is that the limiting currents at all investigated temperatures visible in Fig. 4 are caused by flooding and hence blocking of the reaction sites in the cCL, as correctly suggested by Kuwertz et al.[7] The differences between the water contents in the aCL and cCL, and hence the gradient within the membrane in between both catalyst layers, is
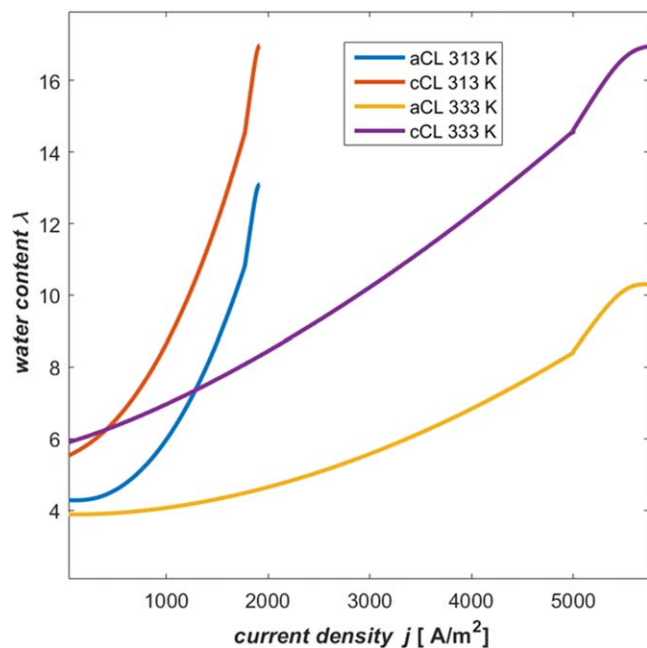
Figure 5. Average water content in the aCL and cCL at 313 K and 333 K as function of current density.

more strongly pronounced in the 333 K case compared to the 313 K case, while the cCL is well humidified in both cases. The markedly higher membrane humidification levels lead to a decrease in the ohmic resistance of the membrane according to Eq. 19, explaining why at 40 K the potential remains almost constant despite increasing current densities within the ohmic regime of both the simulation results and the experimental data of Kuwertz et al.[7] The reason for the lower aCL water content in the 333 K case is the higher saturation pressure of water, which leads to a higher driving force for the evaporation of water out of the membrane and aCL into the aGDL. Due to this driving force, more water is being transported into the anode compartment leading to a stronger concentration gradient of water within the membrane. As soon as water starts to condensate in the cCL, λ_{cCL} surpasses the gas-phase equilibrium value of 14, and the concentration gradient within the membrane, and hence the water crossover, increases further. This becomes obvious when looking at the molar flow rate v_{H_2O} of water crossing over from the cathode to the anode considering the diffusive flux as well as the osmotic drag depicted in Fig. 6 as a function of the current density for the 313 and 333 K simulation. The crossover in the 333 K case is almost 4 times as high as in the 313 K simulations for the above discussed reasons.

As a consequence, more water coming from the electrochemical reaction, and a hence higher current density, is necessary to compensate for the crossed over fraction, so that the flooding process is stretched over a wider current-density interval at higher reactor temperatures, explaining the above discussed phenomena of a slower onset in the limiting behavior at 333 K in comparison to the 313 K case in Fig. 4.

These results illustrate that even when flooding is causing the observed limiting behavior, the humidification, being strongly influenced by the thermal management of the cell, still has a significant impact on the reactor performance. The significant impact of this insight on the feasibility of a technical application becomes clear, when comparing the cell potentials in the experiments of Kuwertz et al.[7] in the ohmic regime at a current density of 3000 A m^{-2} for 40 and 333 K. Following a similar calculation as carried out by Bechtel et al.,[12] the difference of about 300 mV in the cell potential at these two temperatures would correspond to annual savings of more than 6 million Euro in an exemplary industrial application of the HCl oxidation within the MDI production site in
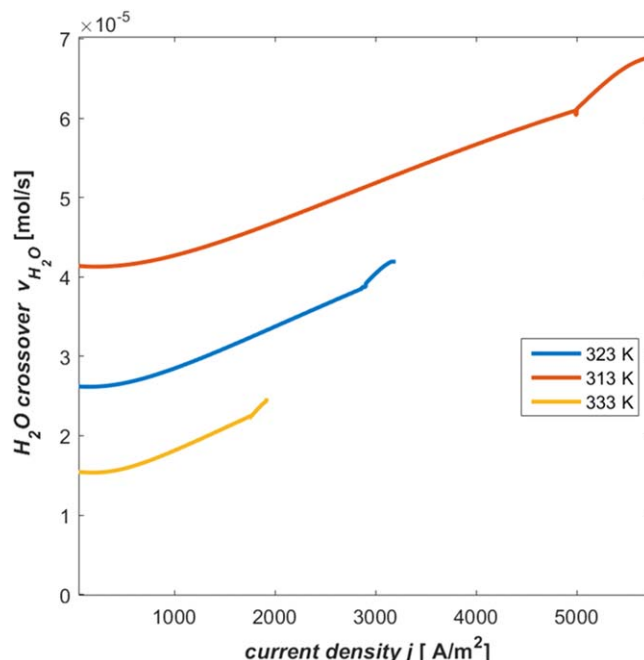

Figure 6. Water crossover through the membrane as a function of the current density for the 313, 323 and 333 K simulation. The slight discontinuities at the onset of the limiting currents are due to the solution switching between a partially saturated and non-saturated state as a consequence of the flooding process leading to numerical artefacts.

Antwerp, underlining the importance of understanding the physical mechanisms leading to these above discussed experimentally observable phenomena.

The role of thermal management.—As discussed above, thermal management plays a significant role in the performance of the HCl gas-phase oxidation reactor. For this reason, and to assess the sensitivity of the reactor performance on its temperature in general, Fig. 7 displays the same polarization curves as Fig. 4, but now with an increased thermal resistance of $R = 0.8$ K/W compared to the
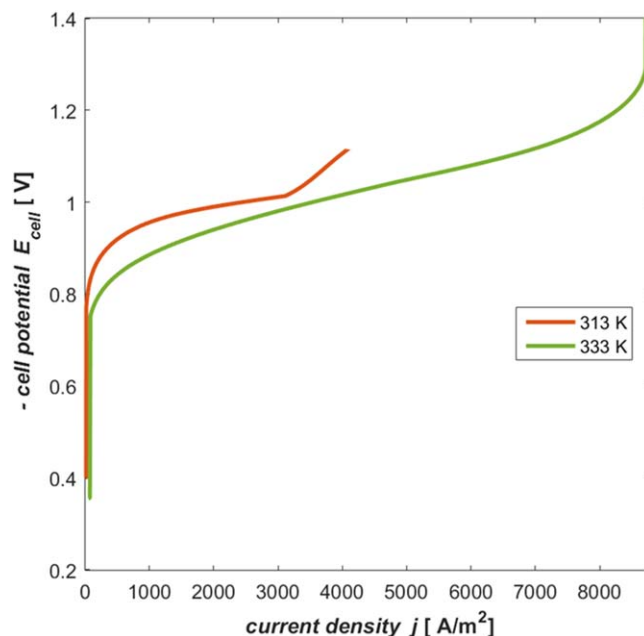

Figure 7. Polarization curves at 313 K and 333 K simulated with a thermal resistance of 0.8 K W^{-1}.
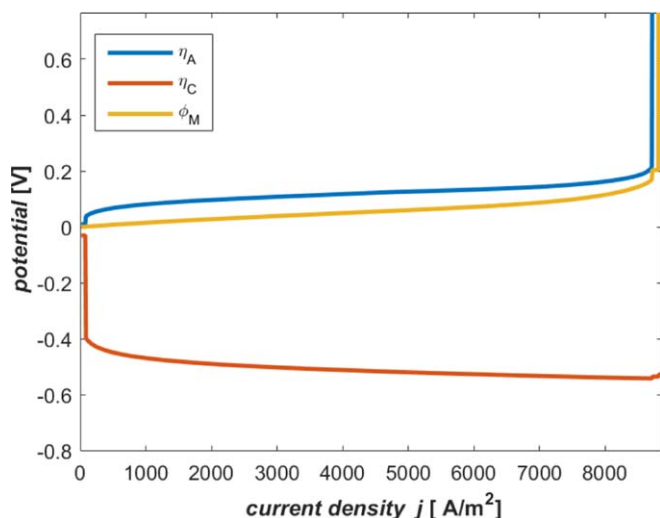
Figure 8. Anode and cathode overpotential as well as the potential loss in the membrane as a function of the current density for the 333 K simulation with a thermal resistance of 0.8 K W^{-1}.

standard resistance of 0.294 K W^{-1} given in Table III. At this value, the cause of the limiting behavior in the 313 K simulation remains to be flooding of the cCL although, as the slower onset in the limiting current indicates, it is on the verge to switch towards membrane dehydration. Furthermore, the limiting current of 4000 A m^{-2} is now almost identical to the experimentally determined one from the work of Kuwertz et al.[7] At temperatures of 333 K and beyond, already a 30% increase in the thermal resistance compared to the standard value given in Table III leads to dehydration of the membrane, which is even stronger pronounced at the here investigated thermal resistance of 0.8 K/W as can be seen in the polarization curve by the steeper slope in the ohmic regime and the sharp onset of the limiting current as a consequence of the water content in the membrane falling below the percolation threshold.

The membrane dehydration in the 333 K simulation is confirmed in Fig. 8, where the anode and cathode overpotential as well as the potential loss in the membrane are depicted as a function of the current density. While the cathode potential remains almost constant, η_A and ϕ_M are increasing sharply at the limiting current, since the low water content decreases the ECSA in the aCL as well as the proton conductivity in the membrane drastically.

Similar conclusions can be drawn from Fig. 9a where again the water contents in the aCL and cCL are depicted as a function of

current density, and from Fig. 9b, displaying the temperature over the investigated current density interval. After an initial increase in the water content due to the electrochemical production of water increasing with the current density, the above-mentioned effect of a higher crossover due to the incline in the saturation pressure with temperature overcomes the hydrating effect of the oxygen reduction reaction and eventually dehydrates the membrane. Moreover, the increase in the membrane potential and the anode overpotential due to the reduced ECSA and hydrochloric acid concentration in turn raises the reactor temperature, further accelerating the dehydration in an autocatalytic fashion. This explains the significant temperature increase in the 333 K simulation in Fig. 9b. In contrast, at a lower temperature of 313 K, where flooding remains the reason for the limiting behavior in both scenarios and only intermediate current densities of ca. 4000 A m^{-2} are reached, the difference between the feed temperature and the reactor temperature is significantly smaller, not exceeding 17 K. More so, at the standard thermal resistance the reactor temperature changes only by a 2 K in the 40 K simulation and by 7 K in the 333 K simulation over the whole current density interval.

Hence, it can be concluded that already slight changes in the structural parameters or operating conditions of the cell can lead to the different physical mechanism causing the observed limiting behavior, especially at operating temperatures of 333 K and beyond.

Outlook on reactor optimization strategies.—In an industrial application of the gas-phase electrolysis of HCl, operation at higher current densities than the ones achieved experimentally so far would translate into significant material and hence financial savings, and would also reduce the environmental impact of such a process. For this reason, the insights about the physical mechanisms discussed in the previous sections are utilized below to derive exemplary strategies on how to control the reactor humidification and temperature in a way that both flooding and membrane dehydration are postponed and the limiting behavior is shifted to significantly higher current densities.

As shown before, especially at higher temperatures the significant gradients in the membrane can impede the overall reactor performance up to the point where the water content in the membrane falls below the percolation threshold, leading to a limiting current. Hence, it seems to be promising to employ thinner membranes that allow for more water crossover into the anode compartment. Moreover, this also mitigates the flooding of the cCL due to a more effective water removal and is expected to reduce the overall cell potential due to higher conductivity in the membrane and increased ECSAs in the aCL. These considerations are confirmed by simulative results displayed in Fig. 10, where the polarization curve for a standard
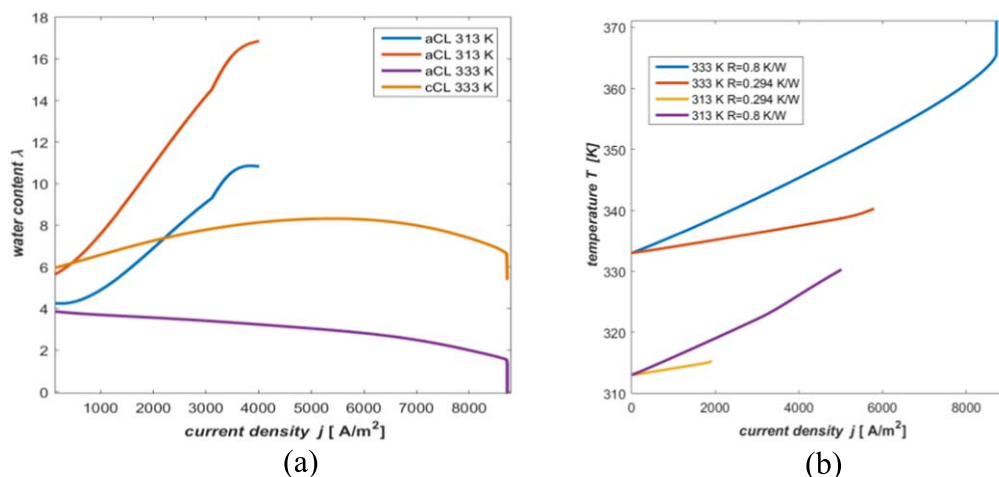

(a)

(b)

Figure 9. (a) Water contents in the aCL and cCL ionomer and (b) reactor temperature as a function of current density for 313 and 333 K feed gas temperature and a thermal resistance of 0.8 K W^{-1}.
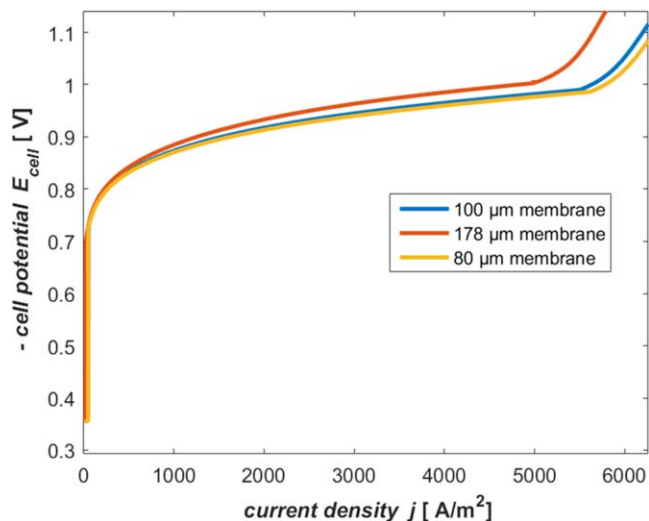
Figure 10. Polarization curves for three different membrane thicknesses at 333 K, employing the standard conditions including the thermal resistance given in Table III.

Nafion®117 membrane, as already depicted in Fig. 4, is compared to two further polarization curves employing membranes with a thickness of 80 and 100 μm, all at a temperature of 333 K.

The thinnest membrane leads to a shift in the onset of the limiting current by ca. 700 Am^{-2} and to slightly lower cell potentials over the whole current density interval compared to the standard Nafion®117 membrane. This difference is even more pronounced in simulations where membrane dehydration causes the observed limiting behavior. These findings are in good agreement with theoretical and experimental insights in the field of classical PEM fuel cells stating that thinner membranes lead to a better water management by reducing the occurrence of membrane dehydration and thus the ohmic resistance. As both Stanic et al.[47] as well as Springer et al.[48] showed, a thinner membrane can significantly increase the limiting current by avoiding flooding of the cCL as well as dehydration of the membrane.

As can be extracted from Fig. 10, both simulations with 100 μm and 80 μm membranes show very similar limiting currents. The effect of an increasing limiting current due to a reduced membrane thickness seems to become less and less relevant below 100 μm, since the saturation level on the anode and cathode side of the membrane approach each other, so that a further reduction only slightly shifts the flooding of the cCL towards higher current densities. It should be noted however, that in scenarios where membrane dehydration becomes the limiting cause, a further reduction in the membrane thickness below 80 μm is expected to lead to more substantial increases in the limiting current densities, in agreement with the above cited literature on classical hydrogen PEM fuel cells. However, as explained below, reducing the membrane thickness beyond a certain degree is not recommended in the specific case of the HCl electrolysis.

Besides the risk of a reduced durability,[49,50] thinner membranes lead to an increase water crossover, which is undesired in the sense that the anode outlet stream should be as dry as possible for reasons of product purification and educt recycling.[5] Additionally, the thinner membrane facilitates crossover of HCl and Cl$_2$, which is poisoning the cathode platinum catalyst.[8] Kuwertz et al.[18] measured OCVs of ca. 700 mV for the ORR in their reactor setup which is significantly smaller than the OCV in classical PEM fuel cells, likely as a consequence of chloride species in the cCL due to crossover. Furthermore, Novac et al.[51] showed that the fraction of the platinum surface covered by chloride species is increasing linearly with the concentration of chloride anions in the electrolyte, underlining again that the membrane thickness should not be reduced too far in order

to reduce crossover. When employing other catalysts that are not sensitive to the presence of chloride anions, like rhodium sulfide, this might not pose a significant problem. For the Pt/C catalyst employed in the experiments of Kuwertz et al.[7] and Martinez et al.[9–11] it is however necessary, to consider additional alternative methods to increase the limiting current density while keeping the crossover of HCl and Cl$_2$ to a minimum.

This becomes obvious when considering that in most hydrogen PEM fuel cell studies current densities of 10000 A m^{-2} and, depending on the humidification conditions and reactor temperature even significantly higher values, can easily be reached even with classical ®Nafion 117 membranes. This is in strong contrast to the experimentally observed maximum value of ca 4500 A m^{-2} in the work of Kuwertz et al.[7] and even the slightly higher limiting currents in the presented simulations herein. The reasons for this are the ability to humidify the anode in PEM fuel cells, which is not feasible in the case of the HCl electrolysis due to the imminent formation of aqueous hydrochloric acid, and the strongly exothermic dissociation of HCl in the aCL, which is more than two times higher than in classical hydrogen PEM fuel cells, thereby leading to a significantly more sensitive and complex heat management problem. For these reasons, below the thermal management issues are elucidated and expanded.

As can be extracted from a comparison of Figs. 7 and 4 the increase in the thermal resistance to a value of 0.8 K W^{-1} led to a markedly higher limiting current, being then caused by membrane dehydration instead of flooding. If one imposes current density dependent thermal resistance, flooding can be avoided at low current densities by imposing a higher thermal resistance and the dehydration of the membrane can be postponed by subsequently decreasing the resistance at higher current densities. Figure 11 shows the polarization curve simulated at a temperature of 333 K with a thermal resistance of 0.8 K W^{-1}, which is already depicted in Fig. 4, in comparison to a polarization curve obtained under the exact same conditions with the exception of a modified thermal resistance R_{mod}, now being a function of the current density.

$$R_{mod} = 0.8 \ \frac{K}{W} \ for \ j \leqslant 7500 \ \frac{A}{m^2} \qquad [30]$$
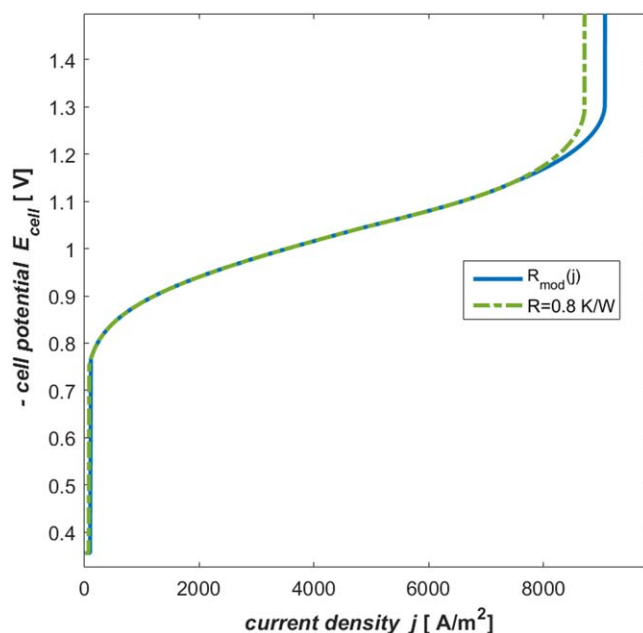

Figure 11. Polarization curve simulated at 333 K with a constant thermal resistance of 0.8 K W^{-1} (green dots) and a current density dependent thermal resistance according to Eqs. 27 and 28.

$$R_{mod} = 0.8 - \frac{\left(j - 7500\frac{\text{A}}{\text{m}^2}\right)}{10300\frac{\text{AW}}{\text{Km}^2}} \; for \; j > 7500 \; \frac{\text{A}}{\text{m}^2} \qquad [31]$$

Up to a current density of 7500 A m^{-2}, the thermal resistance and hence the polarization curves in both scenarios are identical and flooding, as it occurs at the standard thermal resistance as displayed in Fig. 4, is successfully avoided. At higher current densities, the thermal resistance is decreased linearly to reduce the reactor temperature and hence mitigate the dehydration of the membrane, according to Eq. 31. In an experimental setup this could be realized by increasing the flowrate of the cooling medium or a similar effect would be achieved by changing the temperature of the coolant.

The difference in the limiting current as a consequence of the modified thermal resistance is ca. 300 A m^{-2}. Fundamentally however, this modified operational mode can be used to reach significantly higher current densities. It has to be considered though that at the reactant flow rates given by the experimental setup of Kuwertz et al.,[7] a current density of 10000 A m^{-2} is equivalent to a conversion of 77%. Hence, at these high current densities mass transfer effects might play a significant role and can limit the current even though flooding and membrane dehydration are successfully avoided. To prove that it is possible to utilize the insights about the effect of the thermal management and the water balance on the performance of the electrochemical cell to reach significantly higher current densities, the mass transfer effects are circumvented by increasing the anode and cathode feed flow rate by 30% and by reducing the GDL thickness from 400 to 200 μm in the following simulation. This alone does not solve the flooding and dehydration challenge. However, combining the positive effects of a reduced membrane thickness of 120 μm, a tradeoff between higher reactant crossover and increased ohmic losses at very thin or very thick ionomers respectively, and a current density dependent thermal resistance

$$R_{mod} = 0.8\frac{\text{K}}{\text{W}} \; for \; i \leqslant 7800 \; \frac{\text{A}}{\text{m}^2} \qquad [32]$$

$$R_{mod} = 0.8 - \frac{\left(i - 8000\frac{\text{A}}{\text{m}^2}\right)}{15500\frac{\text{AW}}{\text{Km}^2}} \; for \; i > 8000\frac{\text{A}}{\text{m}^2} \qquad [33]$$

the polarization curve shown in Fig. 12 can be obtained. The limiting current is now more than 90% higher than in the simulation with the standard thermal resistance, which is also included in Fig. 12 for reasons of comparability. Interestingly, neither flooding nor membrane dehydration is now at cause for the observable limiting behavior at ca. 11000 A m^{-2} but rather a third mechanism; the kinetic limitation of the HClOR as briefly discussed in the introduction and described in more detail in Refs. 12

This becomes clear when looking at the anode overpotential and the membrane potential losses in Fig. 13 compared to Fig. 8 where membrane dehydration is causing the limiting behavior, the membrane potential now doesn't exceed 150 mV and is significantly smaller than the anode overpotential that becomes dominant at a current density of 10500 A m^{-2}. Furthermore, the cathode overpotential remains almost constant at these high current densities, underlining that also flooding is successfully avoided. The strong increase in the anode overpotential is caused by the surface coverage of the anode catalyst reaching its saturation value as can be extracted from Fig. 14.

At this point, higher overpotentials don't accelerate the reaction any further because the purely chemical Tafel step in the microkinetic reaction mechanism of the HClOR is limiting the overall reaction rate.[12] While at current densities below 10000 A m^{-2} membrane dehydration and flooding of the cCL are the main
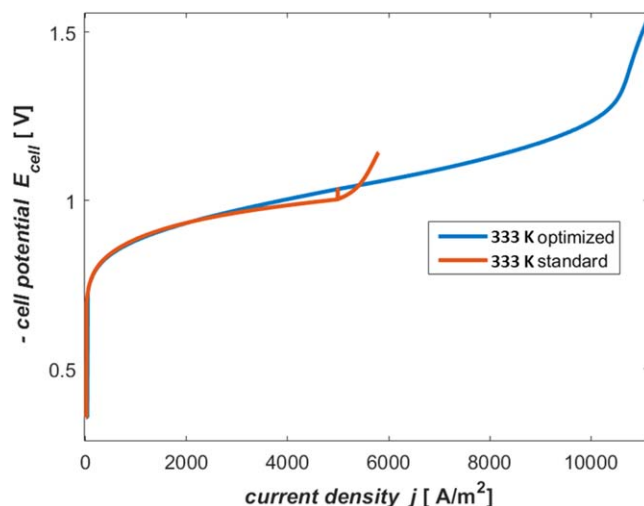

Figure 12. Polarization curve simulated at 333 K with a constant thermal resistance of 0.294 K W^{-1} (red) and the optimized reactor operation with a current density dependent thermal resistance according to Eqs 29 and 30 as well as a reduced membrane and GDL thickness combined with an increased feed flowrate.

concern for the overall reactor performance, at higher current densities the kinetic limitations of the HClOR that so far have only been observed in the half-cell experiments of Martinez et al.[9–12] become relevant. As shown in Ref. 12 this can be mitigated by an increase in the catalyst loading so that theoretically even higher current densities than shown in Fig. 12 can be achieved. This final investigation highlights that under certain conditions not only structural and operational aspects that directly concern the water and energy balance of the cell but also the catalyst structure of the aCL, leading to a possible kinetic limitation, have to be considered.

Please note that the reaction limited currents in the experiments of Martinez et al.[11] at a reactor temperature of 333 K are lower (ca 10000 A m^{-2}) than the one displayed in Fig. 12. This is due to the fact that Martinez' experiments were carried out at conversions of ca 5% and with a strong convective heat dissipation due to the liquid cathode feed, so that quasi-isothermal behavior can be expected. As Fig. 9 shows, this is not the case in the setup of Kuwertz et al.,[7] mainly due to the significantly higher conversion, so that the
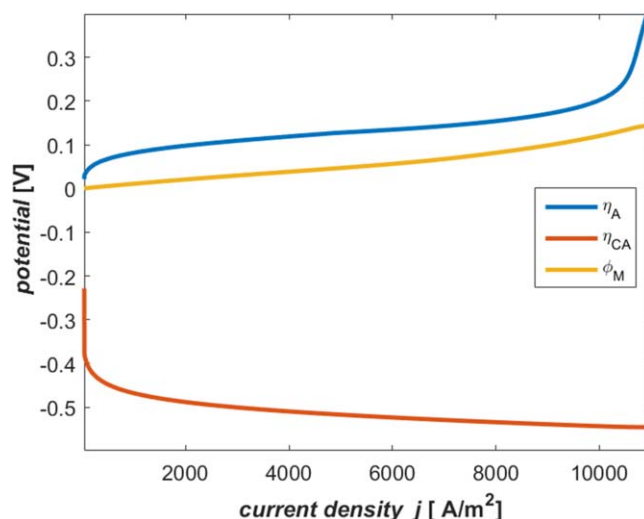

Figure 13. Anode and cathode overpotentials as well as the potential loss in the membrane as a function of the current density for the simulation with an optimized reactor operation.
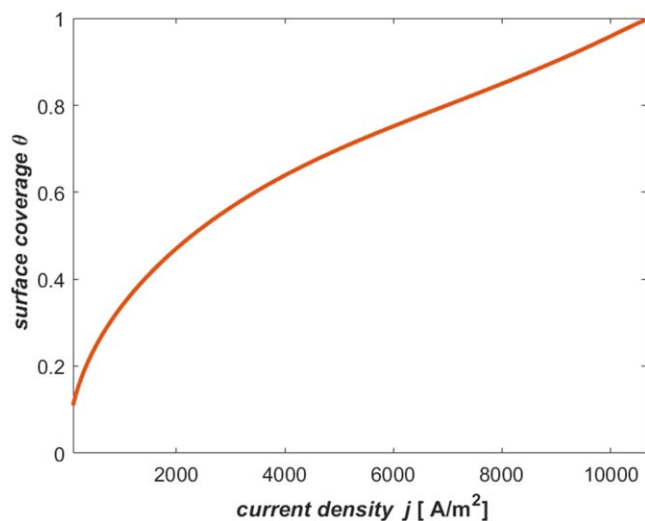
Figure 14. Surface coverage as a function of the current density for the simulation with an optimized reactor operation.

increased reactor temperature leads to a greater rate constant and hence higher limiting currents.

Lastly, the role of mass transfer at these high current densities is investigated to justify the reduction in the GDL thickness and the increase in the O_2 flowrate in the last discussed scenario, as well as to determine if further measures are necessary to prevent the mass transfer from impeding the reactor performance significantly when higher current densities than the so far experimentally achieved ones are desired. Figure 15 displays the partial pressure of O_2 and HCl over the dimensionless GDL length on the cathode and anode side respectively at a current density of 4000 A m^{-2} and 11000 A m^{-2}. Due to the increased flowrate and the stoichiometry of the reaction, the gradient of the O_2 partial pressure remains negligibly small in both cases. At 4000 A m^{-2} the gradient is even slightly positive, which is due to the total pressure increasing in the x direction (please see Fig. 1) at low current densities and correspondingly low saturation levels, due to the stoichiometry of the cathodic oxygen reduction reaction. At the anode, the gradient of HCl, whose reactor inlet flow rate was not increased, is small at current densities lower than 4000 A m^{-2}, which corresponds to the current density range
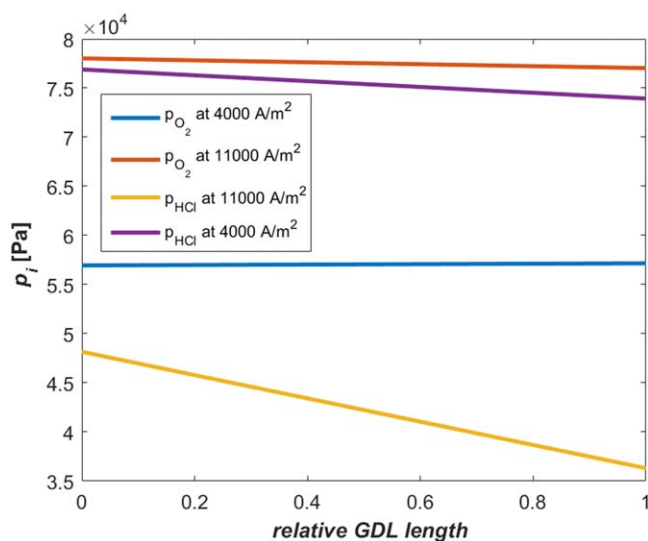

Figure 15. Surface coverage as a function of the current density partial pressures of O_2 and HCl as a function of the relative GDL length at current densities of 4000 and 11000 A m^{-2} for the simulation with an optimized reactor operation.

that Kuwertz et al.[7] reached in their experiments. However, at 11000 A m^{-2}, mass transfer within the GDL seems to play an important, although not yet limiting, role as can be deducted from the distinct gradient in the HCl partial pressure. Hence, while under the conditions in the experiments of Kuwertz et al.,[7] the effect of mass transfer in the GDL is negligible. However, a reduction of the GDL thickness and adjustment of the reactant flow rates should be considered in future experiments when achieving higher current densities is desired.

Finally, the authors would like to emphasize that at these high conversion a 1-D model as employed in the present work cannot be quantitatively predictive. However, the objective of this investigation is to extract geometrical and operational parameters that play a major role in the performance of the reactor, to understand their role in the physical mechanisms that lead to the observable limiting currents and to eventually use that knowledge to propose strategies that allow for operating the process at significantly higher current densities than before. In future investigations, these qualitative insights can be transformed into quantitative predictions of the exact reactor performance by considering the coordinate along the channel and by including a discretized energy balance that is able to account for local temperature gradients.

Conclusion

In this paper, a 1-D multiphase physics-based model of a gas-phase reactor for HCl oxidation to Cl_2 using an oxygen depolarized cathode was developed and compared to the experimental data of Kuwertz et al.[7] Analysis of the predicted polarization curves demonstrated that the observed limiting current is mainly a consequence of two opposing mechanisms, namely flooding of the cathode catalyst layer and dehydration of the membrane and anode catalyst layer. Which one of these mechanisms dominates, strongly depends on the thermal management of the cell. Based on a qualitative comparison and analysis of the experimental and simulated polarization curves it can be stated that under the conditions of Kuwertz experiments, the likely cause is flooding at all investigated temperatures. However, at the highest temperature of 60 K, the effects of membrane dehydration are shown to be already significantly impacting the reactor performance and slight changes in the operating conditions are able to provoke the dehydration of the membrane under otherwise identical conditions. Based on the new understanding of the underlying principles for the limiting behavior, it was possible to adjust operating conditions in a way that the limiting current could be increased by more than 90% by means of avoiding both too high humidification levels leading to flooding and too low humidification levels facilitating membrane dehydration. Interestingly, at these now higher current densities, a third phenomenon, the rate determining desorption step of two Pt-Cl species forming chlorine in the microkinetic mechanism of the HClOR, becomes a limiting factor as well. Lastly, at high current densities of 10000 A m^{-2}, mass-transfer effects where shown to have a considerable, yet not limiting, effect on the reactor performance. In future investigations, the discussed optimizations should therefore come hand in hand with an increased anode catalyst loading to increase the reaction limited current density of the HClOR.

Besides the possibility of operating at higher current densities, structural changes in the reactor, membrane thickness for example, were shown to also reduce the cell voltage markedly at technically relevant current densities, although there are inherent limits. Both, the reduction in the cell potential but also the increase in the limiting current translate into a significant reduction of the operating expenses and investment costs in an industrial scaled application of the HCl gas-phase oxidation. In future investigations, the potential for more efficient reactor operation should be maximized by a rigorous optimization of the above discussed parameters, taking into account possible constraints given by the overall industrial process structure. Furthermore, the presented model as a basis for this optimization should be extended to include effects like the reactant

depletion and water accumulation along the channel, crossover of reactant species, as a next step to make this highly relevant industrial process even more efficient and sustainable.

References

1. M. Zhu, X. Xie, K. Wu, A. Najmi, and K. Jiao, "Experimental investugation of the effect of membrane water content on PEM fuel cell cold start." *Energy Procedia*, **158**, 1724 (2019).
2. M. F. Sonnenschein, in *Polyurethanes: Science, Technology, Markets, and Trends,* Wiley Series on Polymer Engineering and Technology (2014).
3. T. Letcher, "Chemistry beyond chlorine." *Chemistry International*, **38**, 28 (2016).
4. J. Pérez-Ramírez, C. Mondelli, T. Schmidt, O. F.-K. Schlüter, A. Wolf, L. Mleczko, and T. Dreier, "Sustainable chlorine recycling via catalysed HCl oxidation: from fundamentals to implementation." *Energy Environ. Sci.*, **4**, 4786 (2011).
5. S. Bechtel, T. Vidaković-Koch, and K. Sundmacher, "Novel process for the exergetically efficient recycling of chlorine by gas phase electrolysis of hydrogen chloride." *Chem. Eng. J.*, **346**, 535 (2018).
6. S. Bechtel, Z. Song, T. Zhou, T. Vidaković-Koch, and K. Sundmacher, "Integrated process and ionic liquid design by combining flowsheet simulation with quantum-chemical solvent screening." *Comput. Aided Chem. Eng.*, **44**, 2167–2172 (2018).
7. R. Kuwertz, I. G. Martínez, T. Vidaković-Koch, K. Sundmacher, T. Turek, and U. Kunz, "Material development and process optimization for gas-phase hydrogen chloride electrolysis with oxygen depolarized cathode." *J. Appl. Electrochem.*, **46**, 755 (2016).
8. S. Bechtel, T. Vidaković-Koch, and K. Sundmacher, "Energy-efficient gas-phase electrolysis of hydrogen chloride." *Chemie Ing. Tech.*, **91**, 795 (2019).
9. I. G. Martínez, T. Vidaković-Koch, R. Kuwertz, U. Kunz, T. Turek, and K. Sundmacher, "Analysis of a novel chlorine recycling process based on anhydrous HCl oxidation." *Electrochim. Acta*, **123**, 387 (2014).
10. I. G. Martínez, T. Vidaković-Koch, R. Kuwertz, U. Kunz, T. Turek, and K. Sundmacher, "The kinetics of hydrogen chloride oxidation." *J. Serbian Chem. Soc.*, **78**, 2115 (2013).
11. I. G. Martínez, "Hydrogen chloride electrolysis in a polymer-electrolyte- membrane reactor with oxygen-depolarized cathode." *Dissertation* (Otto-von-Guericke University in Magdeburg, Germany) (2015).
12. S. Bechtel, T. Vidaković-Koch, A. Z. Weber, and K. Sundmacher, "Electrochemical gas phase oxidation of hydrogen chloride to chlorine: model-based analysis of transport and reaction mechanisms." *Electrochim. Acta*, **324**, 134780 (2019).
13. A. Z Weber et al., "A critical review of modeling transport phenomena in polymer-electrolyte fuel cells." *J. Electrochem. Soc.*, **161**, F1254 (2014).
14. K. Scott, in *Electrochemical Reaction Engineering* (Academic Press limited, London) (1991).
15. L. Xing, M. Mamlouk, and K. Scott, "A two dimensional agglomerate model for a proton exchange membrane fuel cell." *Energy*, **61**, 196 (2013).
16. V. A. Sethuraman, B. Lakshmanan, and J. W. Weidner, "Quantifying desorption and rearrangement rates of carbon monoxide on a PEM fuel cell electrode." *Electrochim. Acta*, **54**, 5492 (2009).
17. K. C. Neyerlin, W. Gu, J. Jorne, and H. A. Gasteiger, "Determination of catalyst unique parameters for the oxygen reduction reaction in a PEMFC." *J. Electrochem. Soc.*, **153**, 1955 (2006).
18. R. Kuwertz, N. Aoun, T. Turek, and U. Kunz, "Influence of PTFE content in gas diffusion layers used for gas-phase hydrogen chloride electrolysis with oxygen depolarized cathode." *J. Electrochem. Soc.*, **163**, F988 (2016).
19. I. Zenyuk, A. Lamibrac, J. Eller, D. Y. Parkinson, F. Marone, F. N. Büchi, and A. Z. Weber, "Investigating evaporation in gas diffusion layers for fuel cells with x-ray computed tomography." *J. Phys. Chem. C*, **120**, 28701 (2016).
20. A. K. Coker and E. E. Ludwig, in *Ludwig's Applied Process Design for Chemical and Petrochemical Plants* (Elsevier Gulf Professional, Houston, TX) 4th ed., Vol. 1 (2007).
21. T. Vidaković-Koch, I. G. Martínez, R. Kuwertz, U. Kunz, T. Turek, and K. Sundmacher, "Electrochemical membrane reactors for sustainable chlorine recycling." *Membranes*, **2**, 510 (2012).
22. T. F. Fuller, "Solid-polymer-electrolyte fuel cells. PhD Thesis." University of California, Berkeley (1992).
23. A. Kosuglu and A. Z. Weber, "New insights into perfluorinated sulfonic-acid ionomers." *Chem. Rev.*, **117**, 987 (2017).
24. S. Motupally, A. J. Becker, and J. W. Weidner, "Water transport in polymer electrolyte membrane electrolyzers used to recycle anhydrous HCl: I. Characterization of diffusion and electro-osmotic drag." *J. Electrochem. Soc.*, **149**, D69 (2002).
25. N. Stübler, T. Hickmann, and G. Ziegmann, "Electrical and mechanical properties of graphite-based polymer composites for bipolar plates in pem fuel cells."eccm15 -15th European Conf. on Composite MaterialsVenice, Italy 24–28 June, 2012.
26. D. M. Price and M. Jarratt, "Thermal conductivity of PTFE and PTFE composites." *Thermochim. Acta*, **392–393**, 231 (2002).
27. Fluoro-Elastomer Properties data, KB Roller Tech Kopierwalzen GmbH https://www.kbrt.de/en/applications/fluoro-elastomers-fpm-fkm/ (accessed 28th September 2019).
28. R. Krishna and J. Wesselingh, "Review article number 50 – The Maxwell-Stefan approach to mass transfer." *Chem. Eng. Sci.*, **52**, 861 (1997).
29. I. V. Zenyuk, P. K. Das, and A. Z. Weber, "Understanding impacts of catalyst-layer thickness on fuel-cell performance via mathematical modeling." *J. Electrochem. Soc.*, **163**, F691 (2016).
30. A. Z. Weber, R. M. Darling, and J. Newman, "Modeling two-phase behavior in PEFCs." *J. Electrochem. Soc.*, **151**, A1715 (2004).
31. R. J. Balliet and J. Newman, "Cold start of a polymer-electrolyte fuel cell I. Development of a two-dimensional model." *J. Electrochem. Soc.*, **158**, B927 (2011).
32. L. M. Pant, M. R. Gerhardt, N. Macauley, R. Mukundan, R. L. Borup, and A. Z. Weber, "Along-the-channel modeling and analysis of PEFCs at low stoichiometry: development of a 1 + 2D model." *Electrochim. Acta*, **326**, 134963 (2019).
33. J. Zhou, D. Stanier, A. Putz, and M. Secanell, "A mixed wettability pore size distribution based mathematical model for analyzing two-phase flow in porous electrodes ii. model validation and analysis of micro-structural parameters." *J. Electrochem. Soc.*, **164**, F540 (2017).
34. J. T. Gostick, M. A. Ioannidis, M. W. Fowler, and M. D. Pritzker, "Wettability and capillary behavior of fibrous gas diffusion media for polymerelectrolyte membrane fuel cells." *J. Power Sources*, **194**, 433 (2009).
35. A. Kosuglu, A. Kwong, K. T. Clark, H. P. Gunterman, and A. Z. Weber, "Water uptake of fuel-cell catalyst layers." *J. Electrochem. Soc.*, **159**, F530 (2012).
36. M. Eikerling, "Phenomenological theory of electro-osmotic effect and water management in polymer electrolyte proton-conducting membranes." *J. Electrochem. Soc.*, **145**, 2684 (2006).
37. E. N. Balko, J. F. Mcelroy, and A. B. Laconti, "Halogen acid electrolysis in solid polymer electrolyte cells." *Int. I. Hydrogen Energy*, **6**, 577 (1981).
38. A. Kusoglu and A. Z. Weber, "New insights into perfluorinated sulfonic-acid ionomers." *Chem. Rev.*, **117**, 987 (2017).
39. A. Kusoglu, K. T. Cho, R. A. Prato, and A. Z. Weber, "Structural and transport properties of Nafion in hydrobromic-acid solutions." *Solid State Ion.*, **252**, 68 (2013).
40. K. M. Beers, D. T. Hallinan, X. Wang, J. A. Pople, and N. P. Balsara, "Counterion condensation in Nafion." *Macromolecules*, **44**, 8866 (2011).
41. S. Ochi, O. Kamishima, J. Mizusaki, and J. Kawamura, "Investigation of proton diffusion in Nafion®117 membrane by electrical conductivity and NMR." *Solid State Ionics*, **180**, 580 (2009).
42. A. Z. Weber and J. Newman, "Transport in polymer-electrolyte membranes II. mathematical model." *J. Electrochem. Soc.*, **151**, A311 (2004).
43. R. Makharia, M. F. Mathias, and D. R. Baker, "Measurement of catalyst layer electrolyte resistance in PEFCs using electrochemical impedance spectroscopy." *J. Electrochem. Soc.*, **152**, A970 (2005).
44. M. Eikerling and A. A. Kornyshev, "Electrochemical impedance of the cathode catalyst layer in polymer electrolyte fuel cells." *J. Electroanal. Chem.*, **475**, 107 (1999).
45. C. Breitkopf and K. Swider-Lyons, in *Handbook of Electrochemical Energy* (Springer, Berlin, Heidelberg) (2017).
46. J. Zhang, Y. Tang, C. Song, J. Zhang, and H. Wang, "PEM fuel cell open circuit voltage (OCV) in the temperature range of 23 K to 120 K." *J. Power Sources*, **163**, 532 (2006).
47. V. Stanic, J. Braun, and M. Hoberecht, "Durability of membrane electrode assemblies (MEAs) in PEM fuel cells operated on pure hydrogen and oxygen."Int. Energy Conversion Engineering Conf. Portsmouth, VA, United States, 2003.
48. T. E. Springer, T. A. Zawodzinski, and S. Gottesfeld, "Polymer electrolyte fuel cell model." *J. Electrochem. Soc.*, **138**, 2334 (1991).
49. H. Li et al., "A review of water flooding issues in the proton exchange membrane fuel cell." *J. Power Sources*, **178**, 103 (2008).
50. M. Ji and Z. Wie, "A review of water management in polymer electrolyte membrane fuel cells." *Energies*, **2**, 1057 (2009).
51. D. N. Novak and B. E. Conway, "Competitive adsorption and state of charge of halide ions in monolayer oxide film growth processes at Pt anodes." *J. Chem. Soc. Faraday Trans.*, **1**, 2341 (1981).